The Astrophysical Journal Letters, 1000:L24 (15pp), 2026 March 20 https://doi.org/10.3847/2041-8213/ae4964

Energy and Mass Transport Associated with Impulsive Spicular Flows in Solar Coronal Holes

Lei Ni[1,2,3], Jun Lin[1,2,3], Tanmoy Samanta[4], Guanchong Cheng[1,2,3], Yifu Wang[1,2,3], and Robert Erdélyi[5,6,7]
[1] Yunnan Observatories, Chinese Academy of Sciences, Kunming, Yunnan 650216, People's Republic of China; leini@ynao.ac.cn, jlin@ynao.ac.cn
[2] University of Chinese Academy of Sciences, Beijing 100049, People's Republic of China
[3] Yunnan Key Laboratory of Solar Physics and Space Science, Kunming 650216, People's Republic of China
[4] Indian Institute of Astrophysics, Koramangala, Bangalore 560034, India
[5] Solar Physics and Space Plasma Research Centre, School of Mathematical and Physical Sciences, University of Sheffield, Hicks Building, Hounsfield Road, Sheffield, S3 7RH, UK
[6] Department of Astronomy, Eötvös Loránd University, Pázmány Péter sétány 1/A, Budapest, H-1112, Hungary
[7] Gyula Bay Zoltán Solar Observatory (GSO), Hungarian Solar Physics Foundation (HSPF), Petőfi tér 3, Gyula, H-5700, Hungary
Received 2025 November 1; revised 2026 February 11; accepted 2026 February 13; published 2026 March 17

Abstract

How the solar atmosphere is heated from a temperature of about 5000 to 6000 K in the lower atmosphere to about 1–2 MK in the corona has challenged the astrophysical community for nearly 80 yr. The same puzzle exists for the stellar coronae heating as well. In this study, we present a series of findings on solar spicules and their subsequent impact on the corona within a coronal hole environment, characterized by locally open magnetic field lines, combining insights from MHD simulations with observations. We find that the convective and turbulent motions around the solar surface cause extensive shocks and small-scale magnetic reconnection in the lower atmosphere. The combined effects of shock compression and reconnection outflows then drive the formation of groups of spicules with a quasiperiod of about 300 s and a width of ∼200–500 km. The spicule upflows provide an averaged mass flux above 10^{-9} kg m^{-2} s^{-1} in the lower corona to sustain the solar wind in coronal holes, and they continuously trigger further new local slow-mode waves and shocks. These waves supply an energy flux of 10–100 W m^{-2} in the lower corona, and they are dissipated by heat conduction and compression heating to sustain the corona temperature of about 1 MK. The results also indicate that the upward propagating disturbances observed in extreme ultraviolet passbands are caused by both spicule upflows and slow-mode waves and shocks. Our findings help in understanding the long-standing problem of coronal heating and the origin of solar winds in coronal hole regions.

Unified Astronomy Thesaurus concepts: Solar coronal holes (1484); Solar coronal heating (1989); Solar spicules (1525); Solar coronal waves (1995)

Materials only available in the online version of record: animations

1. Introduction

In the Sun's core, nuclear reactions generate immense energy. While the core reaches an extreme temperature of about 15 MK, it cools significantly to around 5000–6000 K at the solar surface. Inexplicably, above the lower solar atmosphere, the temperature sharply rises to about 1–2 MK in the corona. This puzzling behavior, often referred to as the coronal heating problem, also exists for the stellar coronae. Solving this puzzle involves answering the questions of how the energy is transported up into the corona and then how it is converted into heat over an altitude range of several solar radii. Particularly, in a coronal hole, regions on the Sun where the plasma density and temperature are lower than the surrounding, and the magnetic fields there are usually open in the corona (C.-Y. Tu et al. 2005; S. R. Cranmer 2009). Ubiquitous magnetohydrodynamic (MHD) waves in the solar atmosphere are a major group of candidates for solar plasma heating (R. Erdélyi & V. Fedun 2007; R. J. Morton et al. 2012; J. Liu et al. 2019). The convective and turbulent motions around the solar surface generate a copious supply of waves. The slow magnetoacoustic waves usually rapidly develop into shocks and damp in the lower atmosphere before they reach the corona (U. Narain & P. Ulmschneider 1996; B. De Pontieu et al. 2004), while fast magnetoacoustic modes reflect and refract as they propagate upward (C. S. Rosenthal et al. 2002). Furthermore, mode coupling occurs where the sound speed equals the Alfvén speed (T. J. Bogdan et al. 2003). Alfvén waves caused by transverse perturbations could possibly carry enough energy up into the corona in the quiet Sun and coronal hole region (S. W. Mclntosh et al. 2011; J. Liu et al. 2019), but further studies are required to verify whether they can supply sufficient energy for heating the active region (H. Tian et al. 2021; D. Yuan et al. 2023). How the transverse waves are dissipated in the corona is another open question (E. Priest 2014).

Coronal holes are considered a prominent source of the solar wind—a continuous stream of charged particles that escape from the lower solar atmosphere (S. R. Cranmer 2009). The fast solar wind originating from coronal holes (A. Krieger et al. 1973; C.-Y. Tu et al. 2005) largely determines the electromagnetic field environment of the heliosphere, impacting the space environment of Earth and the operation of satellites (I. G. Richardson 2018). The coronal hole regions may often cover a significant portion of the Sun's surface, sometimes reaching 30% or more during a solar activity

minimum period (S. R. Cranmer 2009; C. Lowder et al. 2017). To sustain a temperature of several hundred thousand kelvins to 1 MK in the coronal hole region, an energy flux of approximately $1000\,\mathrm{W\,m^{-2}}$ in the chromosphere and $70\ \mathrm{W\,m^{-2}}$ in the corona is required to balance energy losses due to heat conduction and radiative cooling (G. L. Withbroe & R. Noyes 1977).

Small-scale transient spicules are jet-like features that ubiquitously appear in the solar chromosphere and transition region (A. Secchi 1877; B. De Pontieu et al. 2011; T. M. D. Pereira et al. 2012; H. Tian et al. 2014). The characteristics of solar spicules and jet-like features observed in different wavelengths have been summarized in comprehensive review letters (e.g., A. C. Sterling 2000; G. Tsiropoula et al. 2012; Y. Shen 2021). The numerical models and triggering mechanisms of solar spicules have also been discussed. These elongated features connect the cool solar surface to the hot corona, and various MHD waves and Joule heating processes are induced associating with the generation process of spicules. Therefore, they may play an important role in supplying energy and material to the corona (D. M. Hassler et al. 1999; B. De Pontieu et al. 2011; T. Samanta et al. 2019; L. P. Chitta et al. 2023).

The Interface Region Imaging Spectrograph (IRIS) solar observation satellite (B. De Pontieu et al. 2014a) and the Atmospheric Imaging Assembly (AIA) instruments (J. R. Lemen et al. 2012) on board the Solar Dynamics Observatory (SDO; W. D. Pesnell et al. 2012) have provided high-quality observational data to study solar activities and the resulted perturbations. The perturbations manifest as slanted ridges of alternating brightness (or Doppler velocity) in time–distance maps, which are frequently used to analyze the development of a particular coronal structure. These perturbations are generally referred to as propagating disturbances (PDs). The combined observations of IRIS 1400 Å and SDO/AIA 304 and 171 Å indicate that the beginning of quasiperiodical upward PDs in the coronal holes usually coincides with the rising phase of spicules in the lower atmosphere (F. Jiao et al. 2015; T. Samanta et al. 2015; D. Banerjee et al. 2021). Both the slow magnetoacoustic waves and upflows connected with spicules may contribute to the generation of PDs (C. E. DeForest & J. B. Gurman 1998; H. Tian et al. 2012). However, it is still not clear what role they play in generating PDs, respectively. If slow magnetoacoustic waves indeed frequently appear in the corona and cause the PDs observed in extreme ultraviolet (EUV) passbands, the problem then arises as to where they are triggered, since the slow-mode waves generated around the solar surface are usually rapidly damped in the lower atmosphere. The next important question is whether these slow-mode waves could play a significant role in heating the coronal hole regions.

The early one-dimensional simulations investigated how the initiated gas pressure gradient and shock compression triggered spicules (e.g., K. Shibata & Y. Suematsu 1982; A. C. Sterling et al. 1993; B. De Pontieu et al. 2004). Then, advanced two-dimensional radiative MHD simulations further prove that the convective motions can lead to the formation of slow-mode shocks and trigger solar spicules (e.g., V. H. Hansteen et al. 2006; L. Heggland et al. 2011; K. Kesri et al. 2024). These works focus on slow-mode shocks and the formation process of solar spicules below the transition region. So far, the radiative MHD studies of the corona response arising from slow-mode shocks and spicules in coronal holes are rare. In this letter, we investigate the energy and mass transport associated with spicule upflows in coronal holes through radiative MHD simulations and observations. The triggering process of slow-mode waves and shocks and their roles in coronal heating in the lower corona have been analyzed in detail. We also discuss the generation mechanisms of PDs associated with spicules and compare the numerical results with observations. In the next section, we introduce the observational results. The numerical models are described in Section 3. The main results of the model analysis are presented in Section 4. We provide our conclusions and a discussion in Section 5.

2. Observational Results

We used data obtained from coordinated observations with the IRIS satellite and the AIA instrument on board the SDO. The IRIS observation captured a northern coronal hole region, where several polar plumes are clearly visible in AIA images (Figure 1). In this study, we used data obtained during 23:05 UT on 2020 May 17 to 01:15 UT on 2020 May 18. During this period, IRIS observed in sit-and-stare mode. We used Level 2 processed IRIS data, which has been corrected for dark current, flat-fielding, and geometric distortions. All IRIS Slit-Jaw Images (SJIs) were taken with an 8 s exposure time and a cadence of 36.88 s. The pixel sizes of IRIS SJIs are $0\farcs166$; however, we rebinned the image 2×2 pixels in the Y-axis. AIA images were acquired with a 12 s cadence and have a pixel size of $0\farcs6$. AIA pixels are rescaled to match IRIS data for easier comparison. The IRIS SJIs and AIA images were coaligned using IRIS 1400 Å and AIA 1600 Å images, following the method described in T. Samanta et al. (2015). For this study, we primarily used IRIS from the 2796 Å SJI, which is dominated by the Mg II k 2796 Å line. Additionally, we analyzed AIA filtergram images centered at 171 and 193 Å, dominated by Fe IX and Fe XII emissions, respectively. The IRIS 2796 Å passband is sensitive to plasma at temperatures of approximately 10,000–15,000 K. The AIA 171 and 193 Å filters have peak response functions at approximately 0.8 and 1.25 MK, respectively.

Time–distance plots are widely used to analyze propagating features and their dynamics. In this study, we identified several PDs in the AIA 171 and 193 Å running difference (RD) images (Figure 1). The RD images were obtained by subtracting an image taken 2 minutes earlier. To construct the time–distance maps for AIA and IRIS images, we used a wide slit, as marked in panels (C) and (E) of Figure 1. A wide slit was necessary because the signal in AIA channels is relatively weak for off-disk features, and spicules often exhibit transverse motion. To ensure the same spicule structures were captured and to improve the signal-to-noise ratio, we used a slit with a width of 1.92 Mm. The time–distance maps for AIA channels were generated by averaging the intensity along the width of the slit. For AIA 171 and 193 Å, we processed the time–distance maps by removing a smoothed background trend along the time axis (30 minutes) to enhance the visibility of alternating bright and dark ridges. In contrast, for the IRIS 2796 Å channel, we used the maximum intensity along each row of pixels within the slit, as the background intensity is much lower when spicules are absent.

The resulting time–distance maps are shown in Figure 2. The IRIS 2796 Å time–distance maps, which are sensitive to chromospheric plasma, reveal the evolution of several spicules. Meanwhile, the AIA 171 and 193 Å maps show

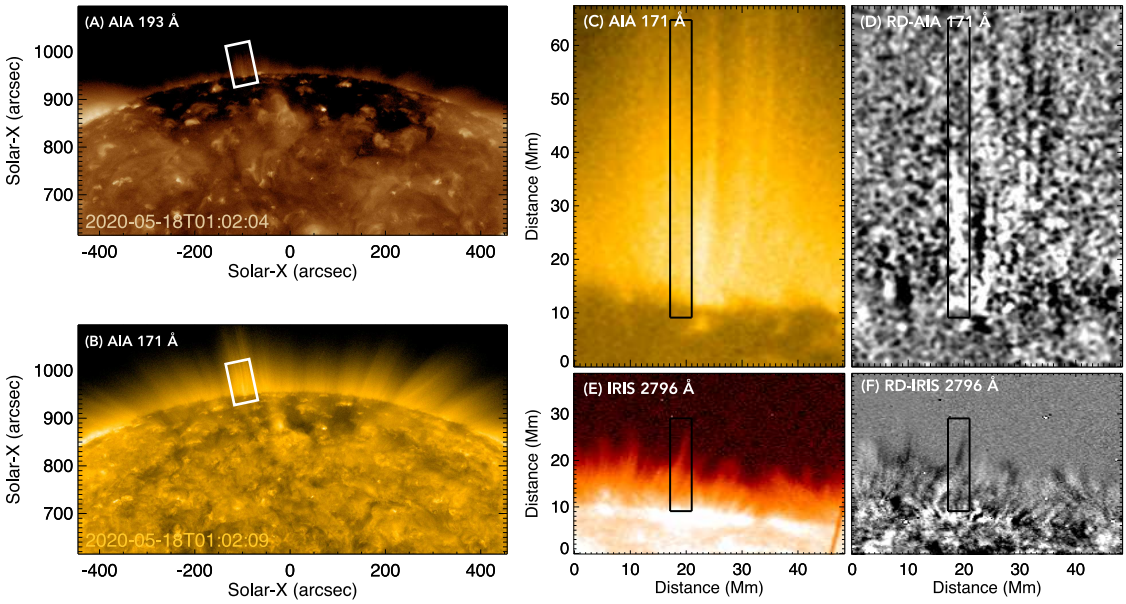

Figure 1. AIA and IRIS images taken around 01:02 UT on May 18, 2020. Panels (A) and (B) show coronal holes in the Sun's south polar region, with the rectangular box marking the location of polar plumes. Panels (C) and (D) present a zoomed-in view and a running difference image of AIA 171 Å, respectively. The RD image highlights a PD, visible as an elongated white strip within the black box. The RD images are obtained by subtracting an image taken 2 minutes earlier. Panels (E) and (F) display the IRIS 2796 Å image and its corresponding RD image, clearly capturing a large spicule at this moment. The *Y*-axis of panels (C)–(F) starts from the bottom of the white box marked in panels (A) and (B). The black rectangular boxes in panels (C) and (E) mark the location of the artificial slits used to generate time–distance plots.

dark and bright ridges extending over longer distances, corresponding to PDs. The temporal evolution of spicules in the IRIS 2796 Å channel exhibits substructures that rise and fall across all passbands, often following a parabolic trajectory, a characteristic feature of many spicules. To highlight the evolution of prominent spicules, we marked their trajectories with white parabolic curves. These same curves are overplotted on the AIA 171 and 193 Å maps, illustrating the connection between the spicular activity observed in the IRIS channel (bottom) and the PDs seen in the AIA channels (top). Notably, the onset of PDs nearly coincides with the rise of the spicular envelope, and the subsequent descent of the spicular envelope is followed by brightenings and the generation of another upward PD in the AIA 171 and 193 Å channels.

3. MHD Models

In the numerical model, we assume the solar plasma is composed of hydrogen and helium. The partially ionized lower solar atmosphere includes hydrogen atoms, helium atoms, electrons, hydrogen ions, and helium ions. In the fully ionized corona, the electrons, hydrogen, and helium ions contribute to the plasma compositions. All the plasma species are assumed to be coupled as one fluid when we solve the MHD equations, and the partial ionization effects can be included in the magnetic induction and energy equations. In this work, we have considered the magnetic diffusion contributed by both electron-ion and electron-neutral collisions, but the ambipolar diffusion is turned off. Based on the open-source NIRVANA code (U. Ziegler 2008), we developed the code by including the partial ionization effects of both hydrogen and helium, and the radiative cooling models have also been updated. Four different radiative cooling models for the convection zone (R. Kippenhahn & A. Weigert 1994), photosphere (W. P. Abbett & G. H. Fisher 2012), chromosphere, and corona (M. Carlsson & J. Leenaarts 2012) are included, respectively. The initial uniform magnetic field is in the *Y*-direction and vertical to the solar surface. In our recent letter (Y. Wang et al. 2025), the details of the solved MHD equations, the formula of the physical magnetic diffusivities, and four radiative cooling models applied from the upper convection zone to the corona have been presented.

We have performed 2.5-dimensional (2.5D) MHD simulations; the numerical domain extends from -6 to 6 Mm in the *X*-direction and from -3 to 22 Mm in the *Y*-direction. The *X*-direction is parallel to the solar surface, and the *Y*-direction is vertical to the solar surface. The region from -3 to 0 Mm in the *Y*-direction represents the upper convection zone. In the two cases presented in Figures 3–9, the numerical resolution is 896×2048. We also performed a higher resolution case with grids 1792×2048. The grid size is 6.7 km in the *X*-direction and 12.2 km in the *Y*-direction. The results for this highest resolution run are presented in Figures 10–12.

The C7 model (E. H. Avrett & R. Loeser 2008) and standard solar model (H. C. Spruit 1974) are applied to set the initial plasma temperature, density, and pressure above the solar surface and in the convection zone, respectively. These initial parameters along the *Y*-direction are plotted in Figure 3(A). The initial magnetic field is uniform, and we ran cases with different strength of magnetic fields, e.g., $B_{y0} = B_0 = 5$ G and $B_{y0} = B_0 = 20$ G. All the initial variables are uniform in the *X*-direction, except that we initiated a small perturbation of the order of 0.01 in density at around $Y = -2.6$ Mm in the convection zone to trigger faster evolution of the whole system, which has also been widely applied in most existing RMHD simulations. Such a small perturbation is applied only once at the beginning, and the quasiperiodic variation in the results is a self-consistent manner caused by convective motions.

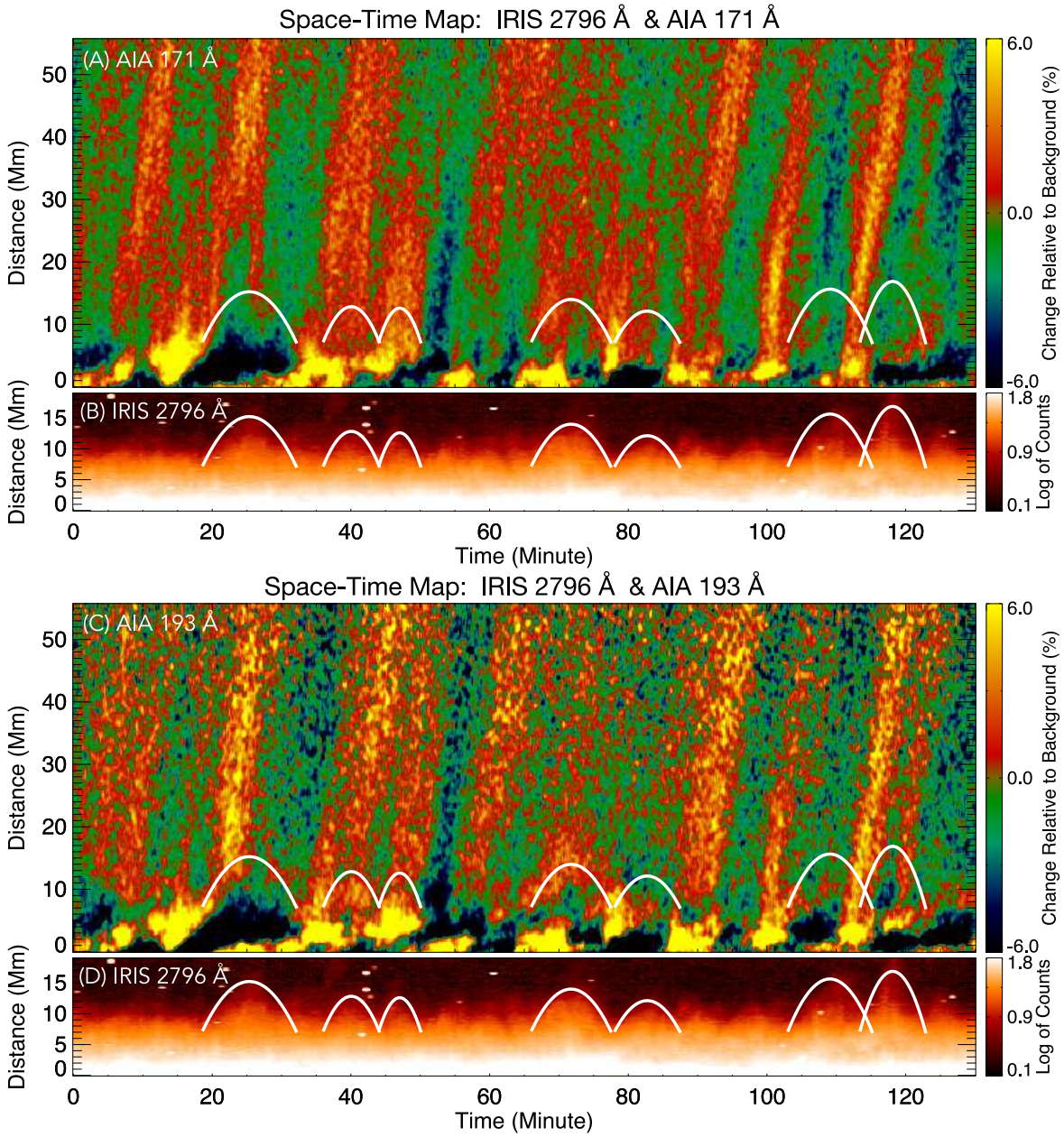

Figure 2. Time–distance maps corresponding to the slits marked in panels (C)–(E) of Figure 1. The slanted bright ridges extending over large distances represent PDs observed in the AIA 171 and 193 Å channels. The IRIS 2796 Å time–distance maps show the evolution of spicules. To highlight the evolution of several prominent spicules, we marked spicular evolutions with white parabolic curves. These same curves are overplotted on the AIA 171 and 193 Å maps to illustrate the connection between spicular activity observed in the IRIS channel in panels (B) and (D) and PDs seen in the AIA channels in panels (A) and (C).

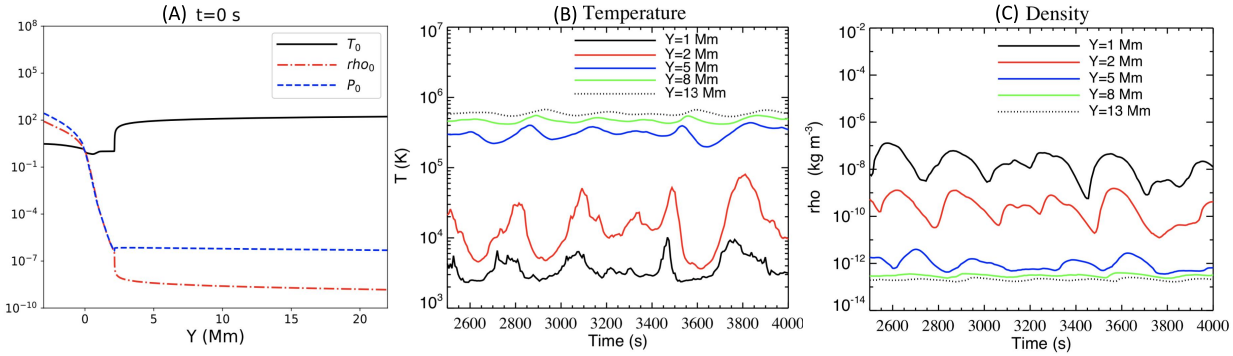

Figure 3. The distributions of plasma parameters at different altitudes. Panel (A) shows the distributions of initial temperature, density, and pressure along the Y-direction, and they are normalized by using the reference values ($T_0 = 6530$ K, $rho_0 = 2.734^{-4}$ kg m^{-3} and $P_0 = 11820$ N m^{-2}) at the bottom of the photosphere. The evolutions of temperature and density at different altitudes are presented in panels (B) and (D), and these values are the averaged ones in the X-direction.

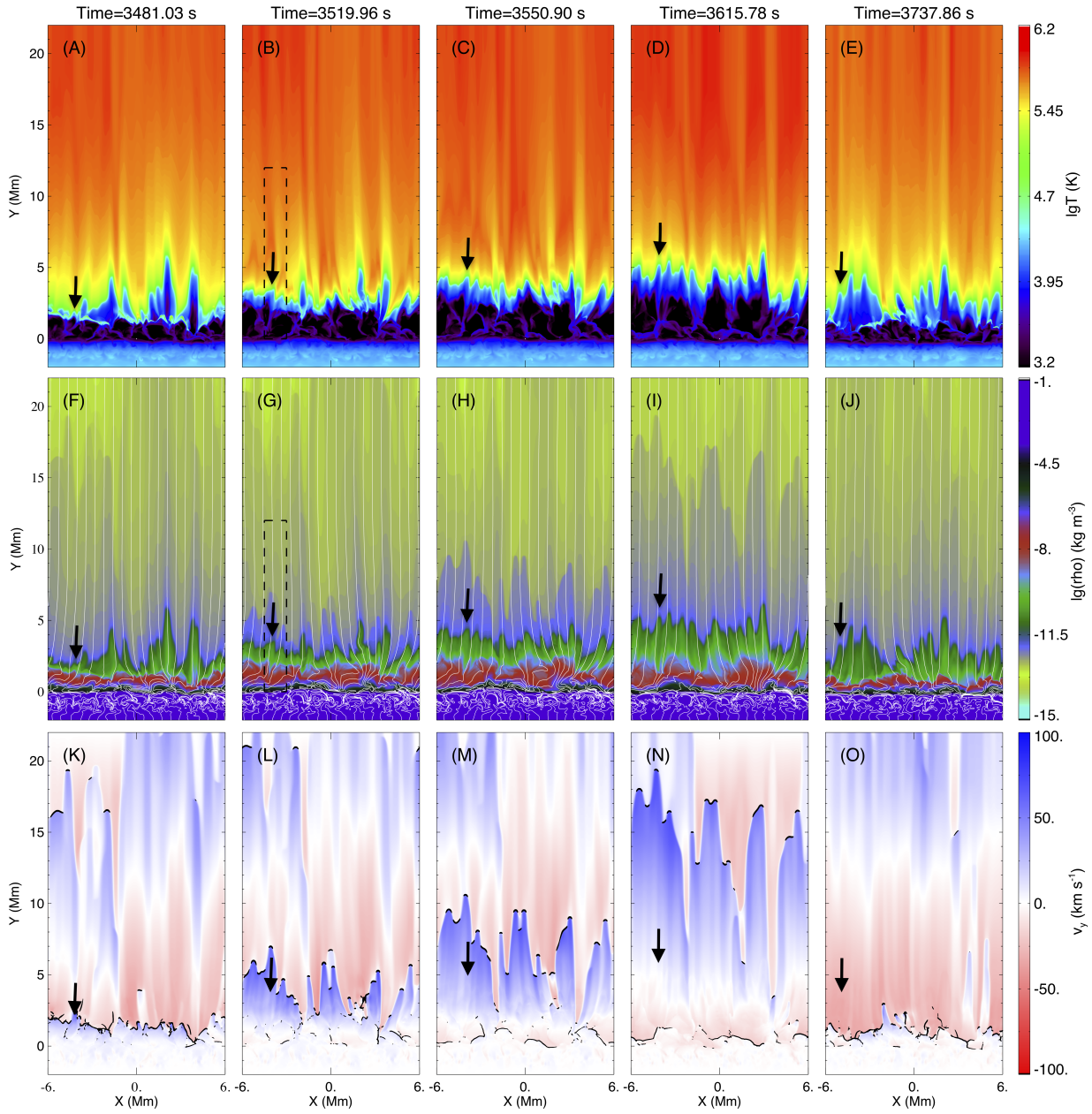

Figure 4. Evolution of spicules and the lower corona above them within a cycle of spicule formation in the 2.5D simulation with the initial magnetic field $B_0 = 5$ G. Distribution of logarithmic temperature (A)–(E), logarithmic density (F)–(J), and velocity in the Y-direction (K)–(O) at five different times are presented. The white solid curves in panels (F)–(J) outline the magnetic field lines. The black dashed boxes in panels (B) and (G) represent the zoomed-in region in Figures 6(A)–(H). The big, thick black arrow in each panel points to the top of one particular spicule with a temperature below 10^5 K. The black contour lines in panels (K)–(O) outline the positions having large values of $-\nabla \cdot V$, indicating the possible invoked slow-mode shocks. The animations of the corresponding temperature distribution, density distribution, and velocity (V_Y) distribution are available in the online journal.

(An animation of this figure is available in the online article.)

The horizontal boundary conditions are periodic. The bottom boundary conditions are inflow, and the top boundary conditions are outflow. At both the bottom and top boundaries, the gradients of the thermal energy, mass density, and parallel components of the magnetic field are set to zero; the perpendicular component of the magnetic field is obtained by divergence-free extrapolation. The gradients of velocities in the X- and Z-directions also vanish at the top and bottom boundaries by assuming $\partial V_x/\partial y = 0$, $\partial V_z/\partial y = 0$. At the bottom boundary, the fluid is only allowed to flow into the computation domain by assuming

$$V_{ybg} = \begin{cases} V_{ybl} & \text{if } V_{ybl} > 0 \\ -V_{ybl} & \text{if } V_{ybl} < 0, \end{cases}$$

where V_{ybg} and V_{ybl} separately represent the velocities at the two bottom ghost layers and at the first two layers inside the simulation domain in the Y-direction. We have also tried some other open boundary conditions; the plasma in the convection zone will always flow dramatically out from the bottom boundary as long as it is allowed to. Therefore, the inflow

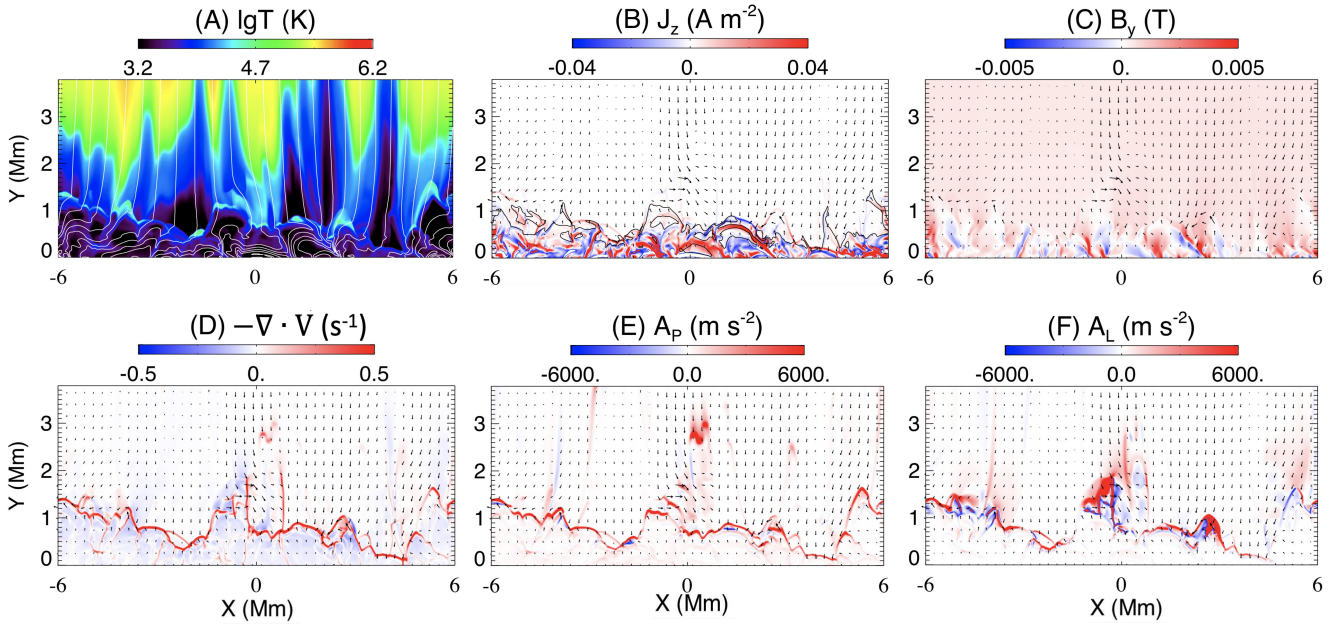

Figure 5. Distributions of different variables in the zoomed lower atmosphere for the 2.5D run with $\mathbf{B_0} = 5$ G at time 3461.07 s, when a bunch of new spicules just start to appear at the altitude between $Y = 0.5$ and 2 Mm. The logarithmic temperature (lgT) (A), current density (J_z) (B), magnetic field in the Y-direction (B_y) (C), the negative divergence of velocity ($-\nabla \cdot V$) (D), the acceleration along the Y-direction contributed by the pressure gradient (A_p) (E), and the acceleration along the Y-direction contributed by the Lorentz force (A_L) (F) are presented. The black thin solid line in panel (B) represents the position where the plasma $\beta = 1$.

boundary at the bottom is our best choice. At the top boundary, the fluid is only allowed to flow out of the computation domain by assuming

$$V_{yug} = \begin{cases} V_{yul} & \text{if } V_{yul} > 0 \\ -V_{yul} & \text{if } V_{yul} < 0, \end{cases}$$

where V_{yug} and V_{yul} separately represent the velocities at the two top ghost layers and the last two layers inside the simulation domain in the Y-direction. We have also added a strong magnetic diffusion coefficient of $\eta_d = 10^9[\tanh(y - 20L_0)/(0.2L_0) + 1]$ around the top boundary, with $L_0 = 10^6$ m, and η_d is in units of square meters per second. Such an outflow boundary and strong magnetic diffusion near the top can prevent plasmas and waves from reflecting back from the top boundary. We have measured the averaged mass flux and energy flux at both the bottom and top boundaries during the period between 3000 and 4500 s. Though the inflow boundary is applied at the bottom, there is no mass and energy flowing into the simulation domain from the bottom boundary during this period. The mass and energy continually flow out of the simulation domain from the top boundary, and the average mass and energy fluxes are about 10^{-9} kg m^{-2} s^{-1} and 100 W m^{-2} respectively, which are close to the values measured from the recent numerical simulation performed by using the advanced MuRaM code (Y. Chen et al. 2025). Such results indicate that the simulations are not influenced by external factors and the numerical results are reliable during the period shown in this letter. However, we should point out that the convective motions obviously become weaker after 5000 s. In future work, the bottom boundary with suitable inflowing mass and energy for balancing the mass and energy loss from the top boundary is required to sustain the convective motions, and we can expect that the longer spicules with faster upflows will be generated.

4. Main Results

4.1. The Simulated Spicule-like Features

The simulated system in all cases is initially not in equilibrium and undergoes significant evolution over time. The convective motions around the solar surface are self-consistently generated. After about 2500 s, the system reaches the state of dynamic equilibrium. Groups of spicules are quasiperiodically ejected upward and fall down, with a period of about 300 s. Distributions of temperature, plasma density, and velocity in the Y-direction at five different times during one period are presented in Figure 4. As shown in this figure, the big thick black arrow in each panel points to the top of one such spicule with a cold elongated plasma jet. It starts to rise at about 3481 s, reaches its maximum height at 3616 s, and then begins to fall (compare panels (A)–(E) and (K)–(O) of Figure 4).

Figure 5(A) shows that such a group of spicules just appears and reaches a height of around 1 Mm above the solar surface. The maximum velocity of the cold chromospheric spicule is above 60 km s^{-1} (see the area indicated by the big thick arrow in Figure 4(K)), which is close to the velocity of the faster type of spicules from observations (e.g., T. M. D. Pereira et al. 2012; B. De Pontieu et al. 2012). During the period between 3460 and 3760 s, we detected 50 spicules, assuming that the width of the spicule is about 200 km. Then, we found that the occurring frequency of the spicule is ~0.1 spicules Mm^{-2} s^{-1}, which is about 5 times smaller than recent measurements from observations (J. Lee et al. 2024).

In our simulations, the ratio between upflowing and downflowing spicules during this period is about 1, which means that the rising spicules always fall back later. However, not all the upflowing plasmas in the spicules return to the solar surface. There is always a small fraction of the ejected material that ultimately reaches the corona. A detailed analysis and descriptions of these findings are presented in the next

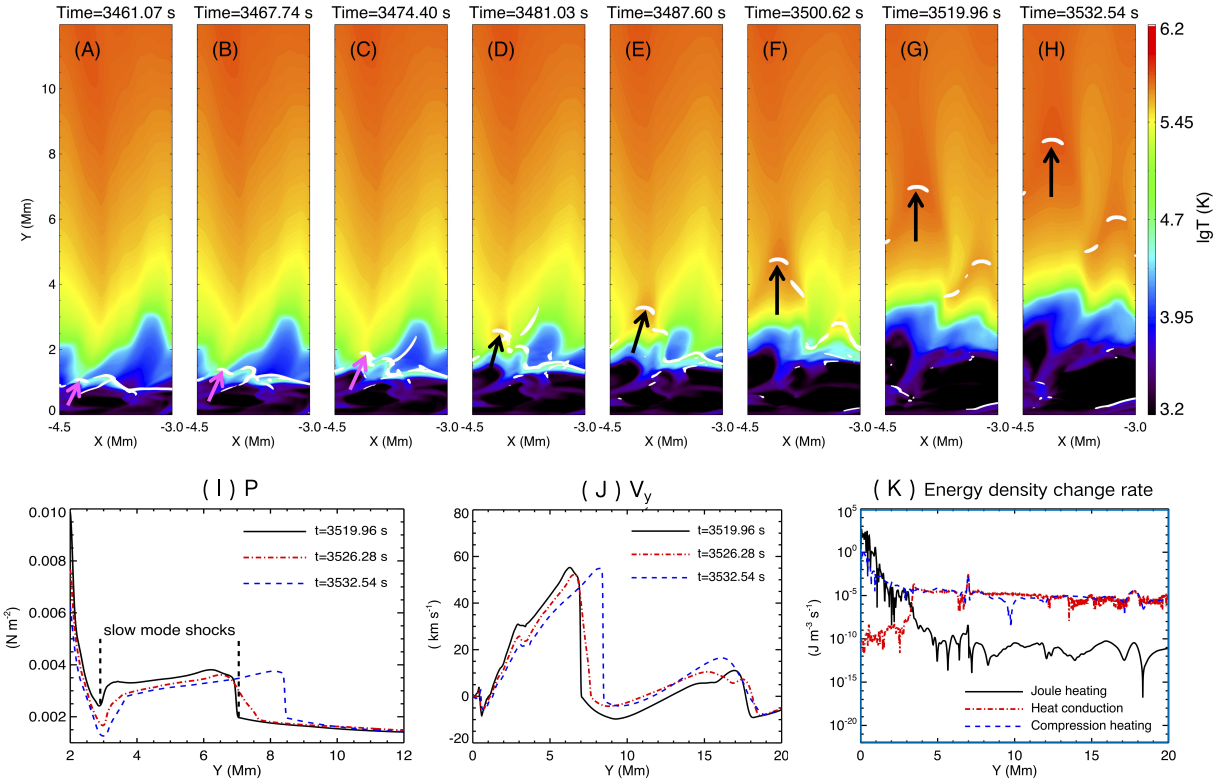

Figure 6. The slow-mode shocks above the spicules in the lower corona. Panels (A)–(H) show the temperature distributions at eight different times in the zoomed-in region inside the black dashed box in Figures 4(B) and (G), where the white contour lines outline the positions having large values of $-\nabla \cdot V$ (shock fronts), the thick pink or black arrows point to the shock front that triggered by plasma upflows during the rising phase of a growing spicule on the left-hand side, and these thick arrows also represent the spicule upflows below the shock front. The distributions of gas pressure P, velocity in the Y-direction V_Y, and the absolute values of the energy density change rate along the Y-direction at $X = -4.15$ Mm are presented in panels (I), (J), and (K). The black solid line, the red dashed–dotted line, and the blue dashed line in panels (I) and (J) mark the values at three different times when the shock fronts are located in the corona. The various lines in (K) indicate the absolute values of the energy density change rate contributed by the Joule heating (ηJ_z^2), the heat conduction ($-\nabla \cdot F_c$), and the compression heating ($-P\nabla \cdot V$) at $t = 3519.96$ s, respectively.

subsection. Based on the observational data from Hα and Ca II K passbands, a previous work (S. Bose et al. 2021) identified approximately 20,000 rapid blueshifted excursions (RBEs) and 15,000 rapid redshifted excursions (RREs), corresponding to about 34% more RBEs than RREs. However, these blue/redshift statistics should not be equated with the occurrence of upflows and downflows. To date, no reliable statistical counts of upflows versus downflows have been established, primarily due to the difficulty of isolating downward motions in Doppler signals. There is one more point that needs to be noted. The downflowing phase of the faster type spicules was normally not observed in Hα and Ca II passbands (T. M. D. Pereira et al. 2012). One of the reasons is that they were heated to higher temperatures during their rising phase, and they were observed to have downflowing phases in the transition region passbands (T. M. Pereira et al. 2014).

The driving process of spicules highly relates to the convective and turbulent motions around the solar surface, which result in various MHD waves (e.g., K. Shibata & Y. Suematsu 1982; A. C. Sterling et al. 1993; B. De Pontieu et al. 2004), complex curved and twisted magnetic fields (e.g., J. Martinez-Sykora et al. 2011; H. Iijima & T. Yokoyama 2017; S. Dey et al. 2022), and magnetic reconnection processes (e.g., T. Yokoyama & K. Shibata 1995; T. Samanta et al. 2019). These physical processes and structures can cause the upward Lorentz force and pressure gradient to push the plasmas upward, and then spicules are formed. As shown in Figures 5(E) and (F), we also find that the acceleration of the spicules at the primary stage is contributed by both pressure gradient and Lorentz force, but the pressure gradient is likely more dominant in most regions below these accelerated spicules.

Figures 5(B) and (C) indicate that many tiny reconnection events appear below 2 Mm when the positive and negative magnetic fields approach each other. These tiny reconnection events change the magnetic topology in their outflow regions and can create strong local Lorentz forces, and the cumulative outflow plasmas can also give rise to the local high-pressure gradients. However, the plasma environment and magnetic structures are very complicated, and they vary rapidly with time. It is normally very difficult to distinguish whether a spicule formation process is dominated by the magnetic reconnection, the shock compression, or other mechanisms, especially when these mechanisms appear simultaneously. As shown in Figure 5(D), the shock compression is also obvious in and below the spicule formation regions. Therefore, the spicule formation process generally relates to both magnetic reconnection and shock compression in our simulations.

4.2. Mass and Energy Transport Associated with Spicules

We observed that the temperature in the corona region increases during the rising phase of spicules and decreases to a

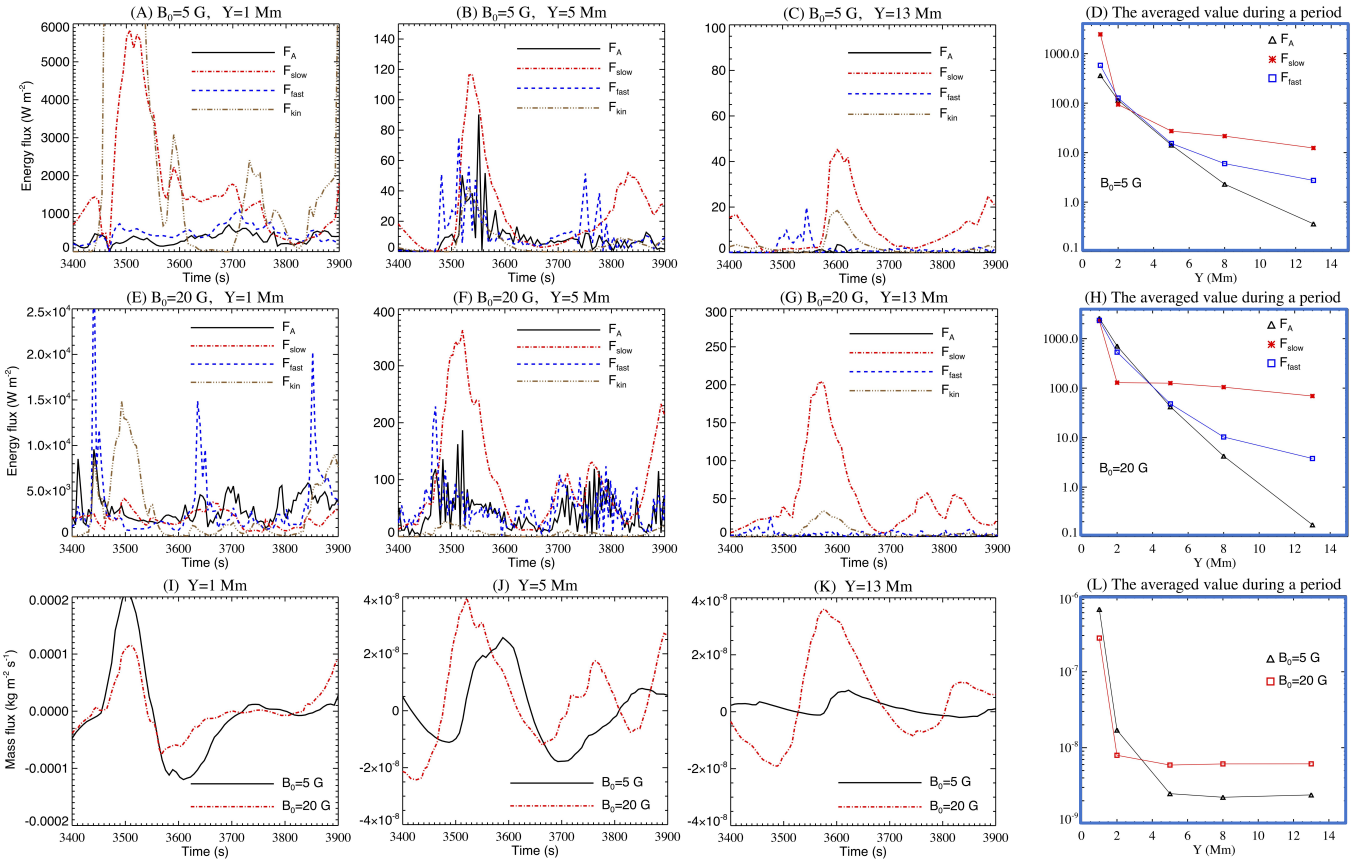

Figure 7. The upward energy fluxes and mass fluxes from the chromosphere to the corona. Panels (A)–(C) show the evolutions of upward energy fluxes carried by Alfvén ($F_{\rm A}$) waves, fast-mode waves ($F_{\rm fast}$) and slow-mode waves ($F_{\rm slow}$), and the upward kinetic energy flux ($F_{\rm kin}$) at $Y = 1$, 5, and 13 Mm, respectively, in the 2.5D run with initial magnetic field $B_0 = 5$ G. The averaged values within a cycle of spicule formation at different altitudes for this case are presented in panel (D). Panels (E)–(G) are the same but with an initial magnetic field of $B_0 = 20$ G, and the averaged values within a cycle of spicule formation at different altitudes for this case are presented in panel (H). The mass fluxes varying with time at $Y = 1$ Mm, $Y = 5$ Mm and $Y = 13$ Mm in the two cases are presented in panels (I)–(K), and the averaged values at different altitudes within a cycle of spicule formation for the two cases are presented in panel (L).

lower value as the spicules fall downward (compare the temperature distributions above the spicule in the top panels of Figure 4). The averaged density and temperature at a particular height fluctuate quasiperiodically (see Figures 3(B) and (C)), and so does the maximum temperature. During the rising phase of these spicules, a small fraction of cool plasmas in the low atmosphere is ejected upward into the corona and heated to the coronal temperature (see the animation accompanying Figure 4). The maximum speed of the rising plasma can reach up to 100 km s^{-1} (see Figures 4(K)–(O)). In the later stage of a characteristic spicular formation period, a fraction of the heated plasma continues to move upward in the corona, with some flowing out through the upper boundary (see Figure 4 and the corresponding animation), while the cooler components fall back onto the solar surface.

Figures 4(K)–(O) show that the slow-mode shocks (the regions with large values of $-\nabla \cdot V$ outlined by black contour lines) are generated both in the lower solar atmosphere and in the corona at much higher altitudes. Figures 6(A)–(H) demonstrate that the slow-mode shocks are locally triggered by the spicular upflows from the lower atmosphere to the corona. Passing through the shock front, one may notice that the distribution of variables such as pressure and velocity in the Y-direction (see Figures 6(I)–(J)) sharply jumps across the shock fronts. The shock front above the spicule is always at the same location as that of the top of the high-speed upflows (see Figures 4(K)–(O)). Since the slow-mode shock is a manifestation of the slow-mode waves in the nonlinear stage, the yet unobservable slow-mode wave in the linear stage should also exist and result from perturbations of upflows in the corona. In previous works (e.g., B. De Pontieu et al. 2004; S. Srivastava et al. 2025), the slow-mode waves or shock waves were assumed to be triggered around the solar surface and then propagate upward into the corona. Here, we show that they can also be directly triggered in the corona, offering a new perspective that addresses the limitation of slow-mode waves and shocks generated in the lower atmosphere, which are believed to be strongly damped before reaching coronal heights.

In addition to the slow-mode waves, other kinds of MHD waves (such as Alfvén and fast-mode waves) are also generated in the solar atmosphere. In Figures 7(A)–(H), the average upward energy fluxes at different altitudes, carried by these waves, are measured on the basis of the differences relative to the initial quantities at the starting time of a spicule formation period (R. Kanoh et al. 2016) (see Appendix A for details). In the chromosphere, the kinetic energy flux ($F_{\rm kin}$) could be larger than the wave energy flux, but $F_{\rm kin}$ decreases rapidly with height. In the case of a stronger background magnetic field ($B_0 = 20$ G), the upward energy fluxes carried by the Alfvén and fast-mode waves ($F_{\rm A}$ and $F_{\rm fast}$) are more than those carried by slow-mode waves ($F_{\rm slow}$) in the

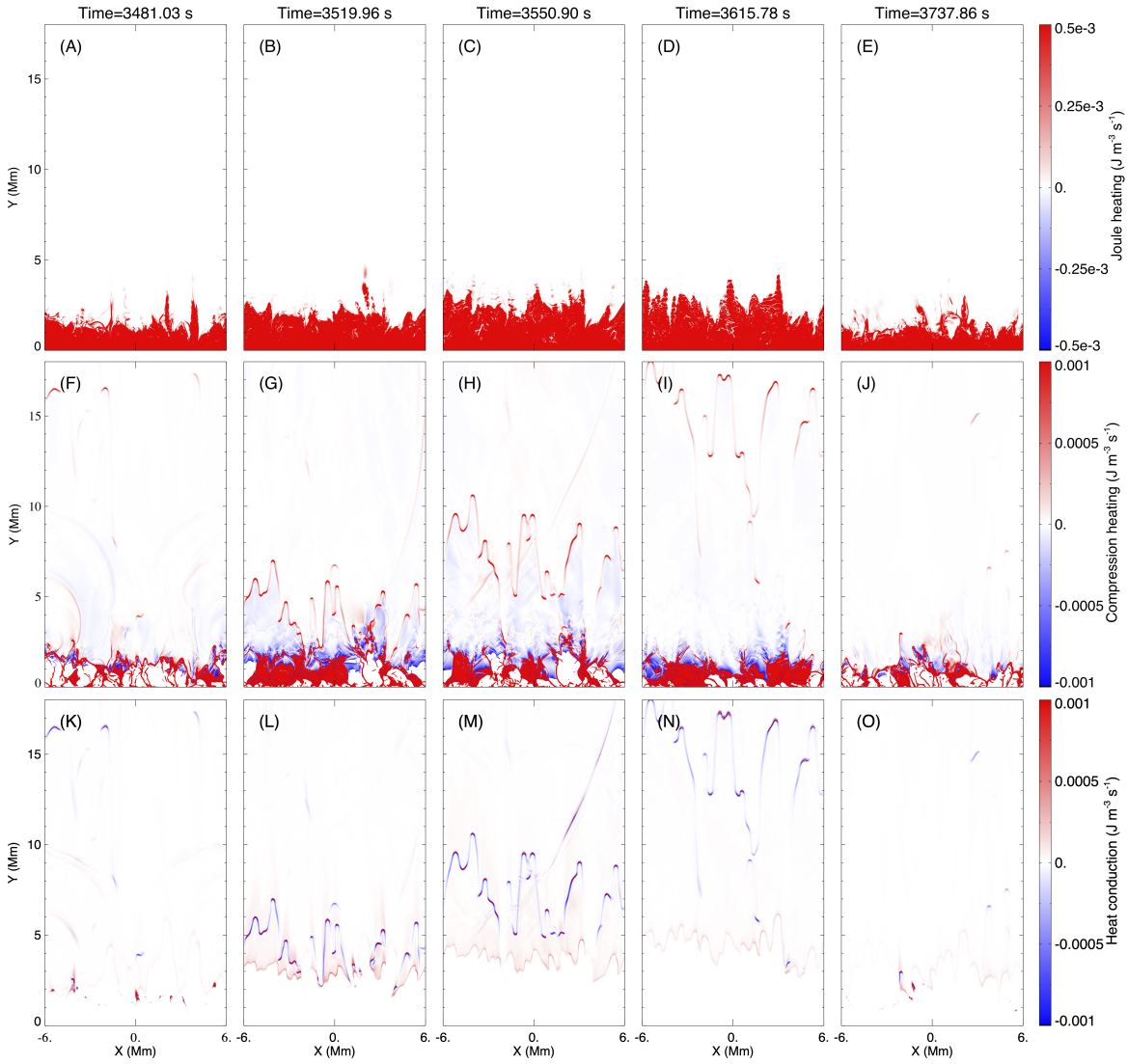

Figure 8. Evolutions of the energy density change rate contributed by three different physical effects within a cycle of spicule formation in the 2.5D run with $\boldsymbol{B_0} = 5$ G. Distributions of the Joule heating (ηJ_z^2) (A–E), compression heating ($-P\,\nabla\cdot\boldsymbol{V}$) (F–J), and heat conduction ($-\nabla\cdot\boldsymbol{F_C}$) (K–O) are presented.

chromosphere. The total average energy flux carried by three distinct MHD waves during a spicule formation period is above 1000 W m^{-2} in the chromosphere in both cases (see Figures 7(D) and (H)). In the corona, $F_{\rm A}$ and $F_{\rm fast}$ still quickly decrease with altitude, but the energy flux carried by the slow-mode wave ($F_{\rm slow}$) decreases more slowly.

Eventually, our finding is that $F_{\rm slow}$ plays the dominant role in the context of carrying upward energy flux in the low corona. In the case of a stronger background magnetic field ($B_0 = 20$ G), the maximum value of $F_{\rm slow}$ exceeds 200 W m^{-2} at $Y = 13$ Mm. During the formation period of spicules from 3480 to 3740 s, the average value of $F_{\rm slow}$ is around 100 W m^{-2} in the lower corona, which is sufficient to balance the energy loss by heat conduction and radiative cooling in the coronal hole (G. L. Withbroe & R. Noyes 1977). In the case of a weaker background magnetic field, $B_0 = 5G$, the average upward energy flux is smaller, but it is still sufficient to sustain a temperature of $\sim$0.6 MK for the coronal hole (see panels (A)–(E) of Figure 4).

The absolute values of the three heating terms evaluated along the Y-axis through a spicule (Figure 6(K)) and the distributions of these heating terms above the solar surface (see Figure 8) indicate that the Joule heating dominates over the other heating mechanisms in the lower solar atmosphere, but it decreases sharply with height. Eventually, the contribution from the Joule heating is overturned by those from heat conduction and compression heating by several orders of magnitude in the corona. Compression heating and heat conduction are two major mechanisms that are usually considered efficient in dissipating shocks and slow-mode waves (D. Banerjee et al. 2021). The magnetic field in the corona is almost unipolar, which causes the absence of the electric current and magnetic reconnection there (see Figures 5(B) and 8(A)–(E)). This result is different from previous simulations about spicule dynamics along the loops in the quiet region on the Sun (J. Martinez-Sykora et al. 2018), which shows that the Joule heating is significant even in the solar corona.

The evolution of the average mass flux at different altitudes in the two cases is presented in Figures 7(I)–(L). The plots show that the plasmas are ejected upward and then most of the rising plasmas eventually fall downward within a cycle of

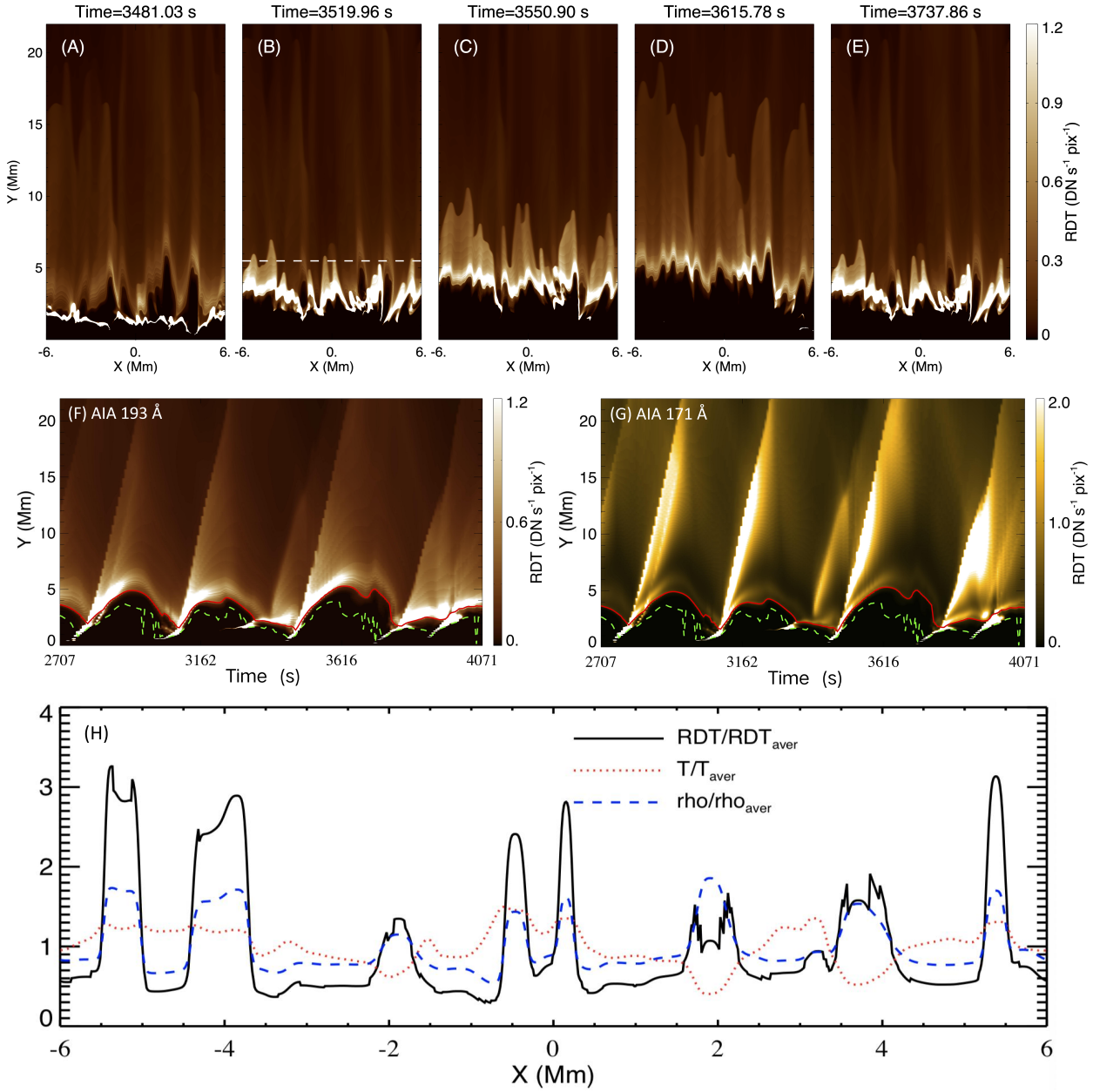

Figure 9. Evolution of the synthesized emission count rate in the 2.5D run with initial magnetic field $B_0 = 5$ G. Panels (A)–(E) show the distributions of the synthesized emission count rate in AIA 193 Å at five different times within a cycle of spicule formation, as in Figure 4. The animations of the corresponding synthesized emission count rate in AIA 171 and AIA 193 Å are available in the online journal. Panels (F) and (G) show the synthesized results varying with time along the Y-direction at $X = -4.15$ Mm. Here, RDT is the synthesized emission count rate, and the unit of RDT is DN s^{-1} pixel^{-1}. The red solid curve and the green dashed curve in panels (F) and (G) correspond to the two locations where $T = 80{,}000$ and 8000 K, respectively. Panel (H) presents the distributions of the normalized synthesized emission count rate in AIA 193 Å (black solid line), the normalized plasma temperature (red dotted line), and normalized density (blue dashed line) along the X-direction at $Y = 5.5$ Mm (the white dashed line in Figure 9(B)) at $t = 3519.96$ s.

(An animation of this figure is available in the online article.)

spicule formation. However, as stated in the first paragraph of this subsection, there is always a small fraction of the ejected plasmas that ultimately reach the corona. The mass flux dramatically drops with altitude in the chromosphere, but it only slightly decreases with altitude in the corona (∼5 Mm above the solar surface), especially in the case of a stronger magnetic field. The mass flux in the chromosphere is higher in the case of a weaker magnetic field, and the situation reverses in the corona. For example, during the period between 3480 and 3740 s, the average mass fluxes at $Y = 13$ Mm are about 2.25×10^{-9} and 6.12×10^{-9} kg m^{-2} s^{-1} in the cases of $B_0 = 5$ and 20 G, respectively. These values are consistent with the mass flux measured in the lower corona of the coronal hole regions (S. R. Cranmer 2009).

4.3. Correlations between PDs and Spicules

It is often debated whether the coronal PDs, a commonly observed phenomenon in coronal hole regions, are plasma flows or slow-mode magnetoacoustic waves. Based on the numerical results, we synthesized the emission count rates in AIA 193 and 171 Å, and the results are presented in

Figure 9, which clearly shows upward PDs. Comparing Figures 4(K)–(O) and Figures 9(A)–(E), one can find that the locations of the bright 193 Å emission region match perfectly with the regions of upflows. Figure 9(H) shows that the enhanced emission in 193 Å of PDs always corresponds to the enhanced plasma density, and the plasma temperature also increases in most of these regions. The enhanced density is attributed to the upflows (see the region inside the black dashed box in Figures 4(G) and (L)), and the increased temperature is caused by the shock compression heating (see Figures 4(B) and 6(G)) together with the dissipation of slow-mode waves in the corona. These results clearly demonstrate that both the upflows and the slow-mode waves contribute to the formation of PDs. When the cool spicules start to slow down and then fall back, part of the EUV emissions just above these spicules also follows a similar path (see Figures 9(F) and (G)). However, we can still see obvious EUV emissions that move upward together with the hot upflows in the corona (see Figures 4 and 9). Therefore, though most of the ejected plasma eventually falls back, a small fraction still continuously moves upward and triggers the newly formed slow-mode waves and shocks, which then cause the upward PDs.

Such a scenario is consistent with the observational results from IRIS and AIA. The evolution of spicules, highlighted with parabolic curves, clearly illustrates that spicules and coronal PDs are generated simultaneously, similar to what we observe in the simulation, as shown in Figure 2. The speed of upward PDs measured from observations is in the range of 100–150 km s^{-1}. According to the results in Figures 9(F) and (G), the speed of upward PDs from numerical simulation is about 100 km s^{-1}. We note that parts of the enhanced emissions in AIA 171 and 193 Å might also have the rising and falling trajectory for some spicules. For example, the spicule in the middle of Figure 2 has a maximum height at about 72 minutes, and parts of the enhanced emissions in 171 and 193 Å look like they are following a trajectory similar to that of IRIS 2796 Å, which is similar to that shown in the synthesized image in Figures 9(F) and (G) from numerical simulations.

5. Conclusions and Discussion

MHD waves supplying energy for heating the solar corona are normally considered to be triggered by the perturbation of plasma and magnetic field in the convection zone or in the lower solar atmosphere. The slow-mode waves generated at such heights usually rapidly develop into shocks and dampen in the chromosphere or the transition region. Therefore, the slow-mode waves were not considered as a plausible mechanism for heating the corona. However, the observed PDs and upflows indicate that the slow-mode waves might frequently occur in coronal holes (D. Banerjee et al. 2021; H. Tian et al. 2021). This work depicts a comprehensive physical scenario about how the convections invoke the formation of spicules, upflows, slow-mode waves, and shocks, and how these perturbations are dissipated to heat the coronal hole regions. Our main conclusions are as follows:

1. The convective and turbulent motions around the solar surface produce multiple shock compression structures and tiny reconnection events in the lower solar atmosphere, and both contribute to the formation of solar spicules. The total acceleration is caused by both the plasma pressure gradient and the upward Lorentz force, but the plasma pressure gradient dominates.

2. A small fraction of the upwardly ejected spicular flows can reach the corona. These spicule upflows continue to rise in the corona, and some portions even flow out of the simulation domain through the upper boundary. They supply a mass flux exceeding 10^{-9} kg m^{-2} s^{-1} in the lower solar corona, which is enough to sustain the solar wind in coronal holes (S. R. Cranmer 2009; J.-B. Dakeyo et al. 2022).

3. The spicular upflows reaching the low corona continue to trigger local slow-mode waves and shocks there. These waves are different from those originating from convection motions at around the solar surface, which can be easily dissipated before reaching the corona. These waves provide an upward energy flux of 10–100 W m^{-2} in the lower corona, and they can be dissipated by heat conduction and compression to heat the original cool spicule plasmas. It is worth noting that the spicule upflows appear quasiperiodically in the corona, followed by a trail of slow-mode and shock waves with concurrent mass flux supplies. Such results demonstrate that slow-mode waves and shocks can play an important role in heating the lower corona in coronal hole regions.

4. The generation of PDs in coronal holes can be attributed to both local enhanced density and temperature. The enhanced density is resulted by upflows, and the increased temperature is caused by the shock compression heating together with the dissipation of slow-mode waves in the corona.

According to previous radiative MHD simulations, the PDs along loops in the quiet-Sun region are also associated with both shock waves and spicular flows (B. De Pontieu et al. 2017). In this work, we more clearly demonstrate how the PDs in the coronal hole region are caused by upflows, slow-mode waves, and shocks. The slow-mode shocks or magnetic reconnection originating from convection motions in the lower atmosphere cause the formation of spicules. Then, the spicule upflows further compress the plasma above them to generate the new slow-mode shocks in the corona. These newly generated shocks in the corona are not those triggered by convective motions. However, in previous letters (e.g., A. C. Sterling et al. 1993; B. De Pontieu et al. 2004), the slow-mode waves and shocks appearing in the corona have always been assumed to have been originally triggered around the solar surface or the lower atmosphere and then propagate into the corona. Based on radiative MHD simulations, we investigated the mass flux and energy fluxes contributed by slow-mode waves and shocks in the coronal hole region. In addition, we find that the Joule heating is much less important than the compression heating and heat conduction in the lower corona of the coronal holes. However, previous simulations of solar spicules along the loops in the quiet Sun region (J. Martinez-Sykora et al. 2018) indicate that Joule heating is still significant in the corona. The different magnetic structures and the strength of the magnetic fields are probably the main reasons for such differences.

The wave and shock signatures and their evolutions related to solar spicules are difficult to distinguish. Better analytic approaches and higher resolution ground-based (e.g., Daniel K. Inouye Solar Telescope; M. P. Rast et al. 2021) and space solar telescopes in various wave bands are crucial for capturing the wave signals in this region. We also note the limitations of this work. The twisting motion of spicules (e.g., T. V. Zaqarashvili & R. Erdélyi 2009; B. De Pontieu et al. 2012, 2014b) is not

considered in the present study. Therefore, the energy flux carried by the Alfvén waves obtained here could be considered as a lower limit. Previous radiative MHD simulations proved that the ambipolar diffusion (the decoupling of ions and neutrals) can amplify the Lorentz force to cause longer and faster spicules (J. Martinez-Sykora et al. 2017). We expect that the ambipolar diffusion can also help to eject more plasmas with higher speed into the corona, further strengthening the formation of slow-mode and shock waves in the corona above the spicules. However, the ambipolar diffusion effect is probably weaker in the coronal hole regions with a weaker magnetic field. It is necessary to determine whether this effect could play an important role in the coronal hole spicule formation process in future work.

There are a substantial number of Sun-like stars (G-type) and stars with a mass smaller than the Sun, for example, M-type and K-type stars, in the Universe. These stars have full convectional outer layers or obvious convection zones. Analogous to the Sun, these stars may produce numerous spicular-type jets in their atmosphere as well. The plasma upflow from the lower atmosphere through spicules is also able to generate the slow-mode wave and shock, and may play an important role in supplying mass for the stellar wind and heating the stellar coronae.

Acknowledgments

We would like to thank the referee for the comments and suggestions made for improving the quality of this work. Lei Ni thanks Prof. Hui Tian from Peking University for the discussions about spicules and PDs, and Dr. Yajie Chen from the Max-Planck Institute for the discussions about boundary conditions. This research is supported by the Strategic Priority Research Program of the Chinese Academy of Sciences under grant No. XDB0560000; the National Key R&D Program of China grant Nos. 2022YFF0503804 (2022YFF0503800) and 2022YFF0503003 (2022YFF0503000); the NSFC grants 12373060 and 11933009; the Basic Research of Yunnan Province in China under grant No. 202401AS070044; China's Space Origins Exploration Program; the Yunling Scholar Project of the Yunnan Province and the Yunnan Province Scientist Workshop of Solar Physics; Yunnan Key Laboratory of Solar Physics and Space Science under grant No. 202205AG070009; We benefit from the discussions of the ISSI-BJ Team "Solar eruptions: preparing for the next generation multi-wave band coronagraphs." This work was also supported by the International Space Science Institute project (ISSI-BJ ID 24-604) on "Small-scale eruptions in the Sun." R.E. acknowledges the NKFIH (OTKA, grant No. K142987) Hungary for enabling this research. R.E. is grateful to Science and Technology Facilities Council (STFC, grant No. ST/M000826/1) UK, PIFI (China, grant No. 2024PVA0043), and the NKFIH Excellence grant TKP2021-NKTA-64 (Hungary). The simulation work was carried out at the National Supercomputer Center in Tianjin, and the calculations were performed on the Tianhe new-generation supercomputer. The numerical data analysis was performed at the Computational Solar Physics Laboratory of Yunnan Observatories. IRIS is a NASA small explorer mission developed and operated by LMSAL with mission operations executed at NASA Ames Research Center and major contributions to downlink communications funded by ESA and the Norwegian Space Centre.

Appendix A
Methods for Calculating the Energy Fluxes

In the simulation domain, the wave energy flux vector can be measured as below:

$$\boldsymbol{F}_{\rm wave} = \tilde{P}\boldsymbol{v} + \frac{1}{\mu_0}(\boldsymbol{B}_b \cdot \tilde{\boldsymbol{B}})\boldsymbol{v} - \frac{1}{\mu_0}(\boldsymbol{v} \cdot \tilde{\boldsymbol{B}})\boldsymbol{B}_b, \tag{A1}$$

where the subscript b represents the background variable, a tilde represents the perturbation from the background conditions, and P represents the plasma pressure (S. J. Mumford et al. 2015). This equation has been widely used and discussed in previous letters (e.g., T. J. Bogdan et al. 2003; S. J. Mumford et al. 2015). In this work, we also employ it to calculate the averaged energy fluxes along the Y-direction, the energy fluxes carried by the slow-mode wave ($F_{\rm slow}$), fast-mode wave ($F_{\rm fast}$), Alfvén wave ($F_{\rm A}$), and the kinetic energy flux $F_{\rm kin}$ along the Y-direction at a particular height can be simply derived as below:

$$F_{\rm slow} = \frac{\int \frac{B_{0y}}{B_0}\mathbf{V}_{\parallel}\delta P dx}{\int dx}, \tag{A2}$$

$$F_{\rm fast} = \frac{1}{\mu_0}\frac{\int B_{0y}\delta B_{\parallel} V_{\perp} dx}{\int dx}, \tag{A3}$$

$$F_{\rm A} = \frac{1}{\mu_0}\frac{\int B_{0y}\boldsymbol{V}_{\perp} \cdot \delta\boldsymbol{B}_{\perp} dx}{\int dx}, \tag{A4}$$

$$F_{\rm kin} = \frac{\int \rho V^2 V_y dx}{\int dx}. \tag{A5}$$

In the above equations, $\delta\boldsymbol{B} = \boldsymbol{B} - \boldsymbol{B}_0$ and $\delta P = P - P_0$. The subscripts 0, $\perp$, and $\parallel$ represent the initial values and the values perpendicular and parallel to the initial magnetic fields, respectively. We used the values at the beginning of a spicule formation period as the initial ones to calculate the related upward (positive) energy flux, as shown in Figures 7(A)–(H), 11, and 12. Similar methods for determining the energy flux carried by MHD waves have been used in previous works (R. Kanoh et al. 2016; Y. Kotani & K. Shibata 2020). The mass flux shown in Figures 7(I)–(K) and Figure 11(E)–(H) is calculated as

$$F_{\rm mass} = \frac{\int V_y \rho dx}{\int dx}. \tag{A6}$$

Appendix B
Synthetic Plasma Emission

The synthetic emission count rates in AIA 171 and 193 Å as shown in Figure 9 are given by

$$\mathrm{RDT} = \int n_e^2 f(\mathrm{T}) dz, \tag{B1}$$

where n_e is the electron density and $f(T)$ is the temperature dependent response function (J. R. Lemen et al. 2012) corresponding to different wavelengths in AIA from the Chianti package (G. Del Zanna et al. 2015). The unit of RDT is

DN s^{-1} $pixel^{-1}$. In our 2.5D simulations, all the variables, including RDT, are uniform in the Z-direction, and we assume that the length scale in the Z-direction is 1 Mm, which is comparable to the size of a spicule.

Appendix C
The Effects of Numerical Resolutions

In order to check the effects of resolutions on numerical results and conclusions, we performed simulations with both lower and higher resolutions for the case with an initial magnetic field of 5 G. The numerical results show that the width of the spicules is narrower, and the length can reach a higher value in the simulation with a higher resolution. When the grid size is 12.2 km in both the X- and Y-directions, the width of the spicule is in the range of ∼200–500 km, and a maximum length of ∼8 Mm (see Figure 4) can be reached. The width of the spicule can reach a very small value of ∼120 km, and the maximum length is above 10 Mm (Figure 10) in the simulation with an extremely small grid size of 6.7 km. The maximum temperature and velocity in the corona region in the higher resolution simulation are both higher, and the corona temperature is also more nonuniform in this simulation (comparing Figures 4(A)–(E) and 10(A)–(E)).

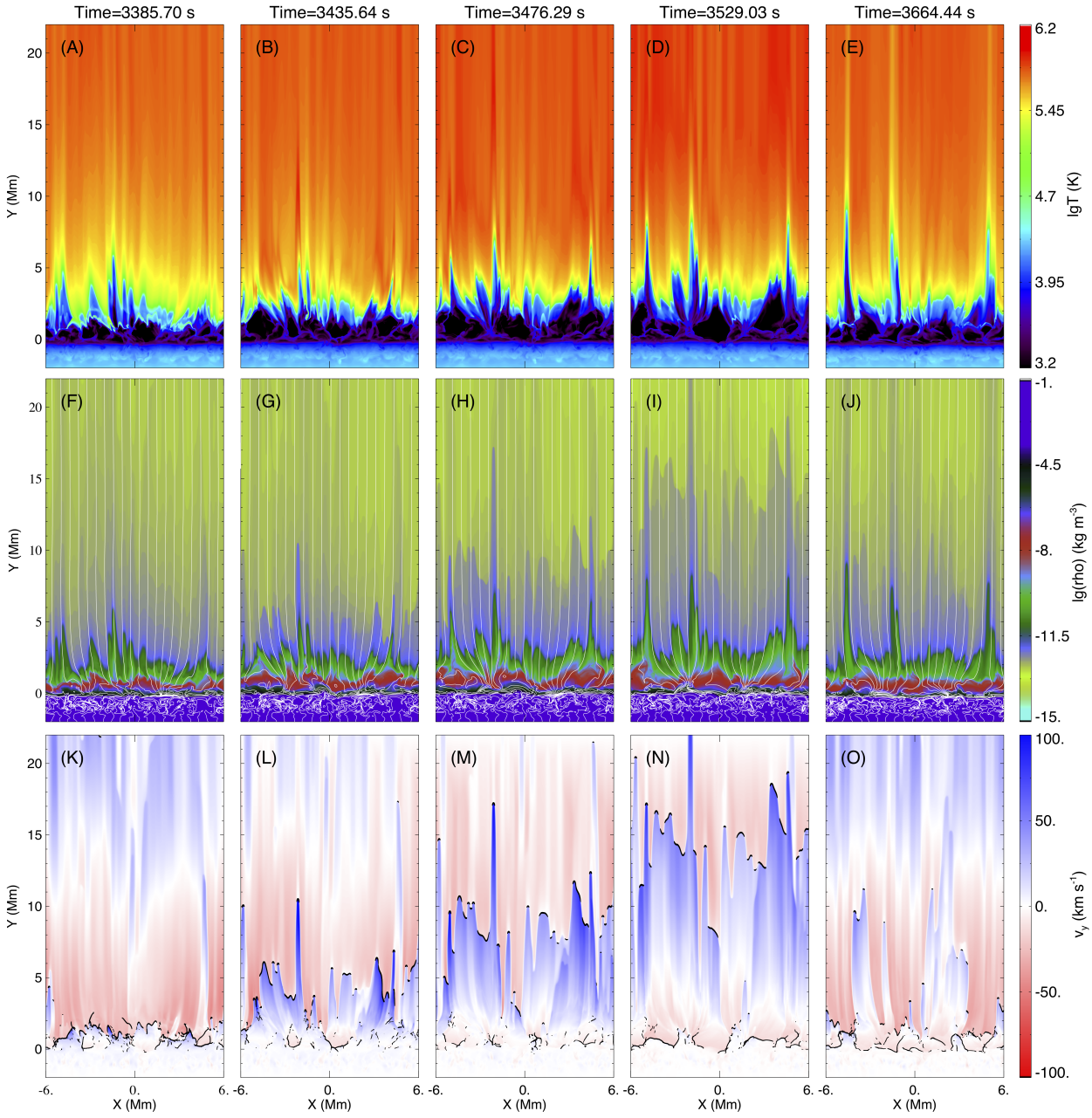

Figure 10. Evolution of spicules and the lower corona within a cycle of spicule formation in the higher resolution 2.5D run. All the initial and boundary conditions in this case are the same as those in the case with initial magnetic field $B_0 = B_{0y} = 5$ G shown in Figure 3. Distributions of logarithmic temperature (A)–(E), logarithmic density (F)–(J), and velocity in the Y-direction (K)–(O) at five different times are presented. The white solid curves in (F)–(J) are for the magnetic field lines. The black contour lines in (K)–(O) represent the regions having large values of $-\nabla \cdot V$ (shock fronts). The animations of the corresponding temperature distribution are available in the online journal.

(An animation of this figure is available in the online article.)

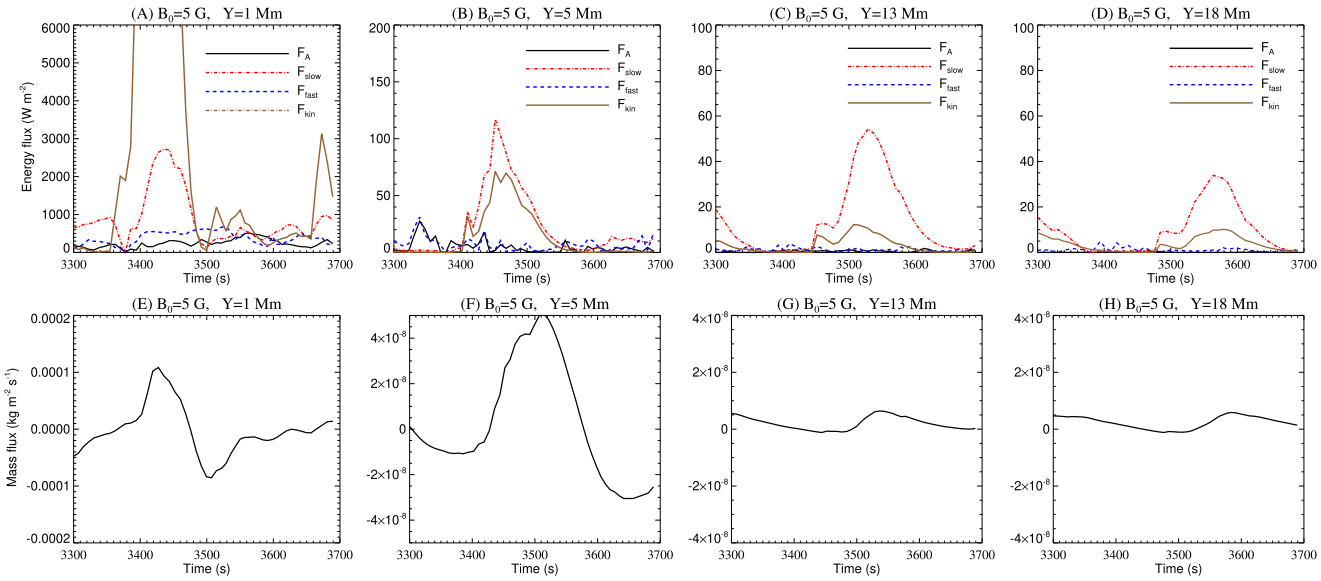

Figure 11. Upward energy fluxes and the mass fluxes from the chromosphere to the corona in the higher resolution case. The energy fluxes carried by Alfvén (F_A) waves, fast-mode waves (F_{fast}), and slow-mode waves (F_{slow}) (A)–(D) and the mass flux (E)–(H) varying with time at Y = 1, 5, 12, and 18 Mm are presented.

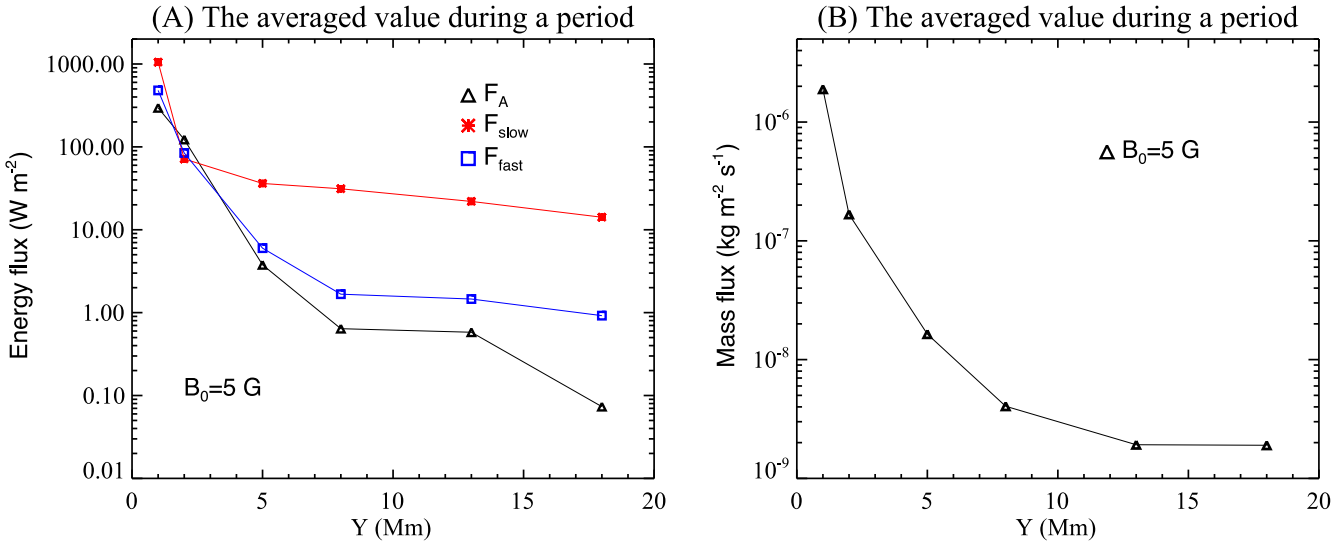

Figure 12. Averaged upward energy fluxes (A) and mass flux (B) within a cycle of spicule formation at different altitudes in the higher resolution case are presented.

According to the methods presented in Appendix A and Equations (A1)–(A6), we calculated the average energy fluxes carried by Alfvén (F_A), fast-mode (F_{fast}), and slow-mode (F_{slow}) waves, and the mass flux at various altitudes for the simulations with different resolutions. The values of the averaged upward energy fluxes, mass flux, and their trends of changing with time and altitudes in the higher resolution simulation (Figures 11 and 12) are close to those from the lower resolution simulation (compare Figures 7, 11, and 12). The upward energy flux carried by slow-mode waves also dominates in the corona region in the higher resolution simulation, as shown in Figures 11(A)–(D) and 12(A). Therefore, our conclusions are not affected by numerical resolution. However, comparing Figures 7(D) and 12(A), one can note that the calculated values in the higher resolution case are relatively larger than those in the lower resolution case. The reason is that the lower resolution case tends to average out or filter out more small-scale variations and details.

Appendix D
The Results from 3D MHD Simulations

We have performed a full 3D simulation to complement this work. The C7 solar atmosphere model is also used to set the initial plasma parameters, and the density stratification occurs in the Z-direction, which is vertical to the solar surface. The initial background magnetic field is assumed to be $B_0 = 10$ G in the Z-direction. The simulation domain spans from -8 to 8 Mm in both the X- and Y-directions, and from -3 to 9 Mm in the Z-direction. The grid number is $96 \times 96 \times 256$. The grid size in the Z-direction is 46.9 km, and it is 167 km in the X- and Y-directions. Therefore, the resolution in this 3D simulation is much lower than that in the 2.5D simulations. However, the spicule-like structures are also formed in this 3D run. We also find that significant heating still appears in the corona above the cold spicule during its rising phase. These heatings might also be caused by slow-mode waves and

shocks, which require future higher resolution 3D simulations to verify.

ORCID iDs

Lei Ni https://orcid.org/0000-0001-6366-7724
Jun Lin https://orcid.org/0000-0002-3326-5860
Tanmoy Samanta https://orcid.org/0000-0002-9667-6392
Guanchong Cheng https://orcid.org/0000-0002-1264-6971
Robert Erdélyi https://orcid.org/0000-0003-3439-4127

References

Abbett, W. P., & Fisher, G. H. 2012, SoPh, 277, 3
Avrett, E. H., & Loeser, R. 2008, ApJS, 175, 229
Banerjee, D., Krishna Prasad, S., Pant, V., et al. 2021, SSRv, 217, 76
Bogdan, T. J., Carlsson, M., Hansteen, V. H., et al. 2003, ApJ, 599, 626
Bose, S., Joshi, J., Henriques, V. M. J., & Rouppe van der Voort, L. 2021, A&A, 647, A147
Carlsson, M., & Leenaarts, J. 2012, A&A, 539, A39
Chen, Y., Peter, H., Przybylski, D., Iijima, H., & Chitta, L. P. 2025, A&A, 702, L4
Chitta, L. P., Zhukov, A. N., Berghmans, D., et al. 2023, Sci, 381, 867
Cranmer, S. R. 2009, LRSP, 6, 3
Dakeyo, J.-B., Maksimovic, M., Démoulin, P., Halekas, J., & Stevens, M. L. 2022, ApJ, 940, 130
De Pontieu, B., Carlsson, M., Rouppe van der Voort, L. H. M., et al. 2012, ApJ, 752, 6
De Pontieu, B., De Moortel, I., Martinez-Sykora, J., & McIntosh, S. W. 2017, ApJL, 845, L18
De Pontieu, B., Erdélyi, R., & James, S. P. 2004, Natur, 430, 536
De Pontieu, B., Title, A. M., Lemen, J. R., et al. 2014a, SoPh, 289, 2733
De Pontieu, B., Mclntosh, S., Carlsson, M., et al. 2011, Sci, 331, 55
De Pontieu, B., Rouppe van der Voort, L., McIntosh, S. W., et al. 2014b, Sci, 346, 1255732
DeForest, C. E., & Gurman, J. B. 1998, ApJ, 501, 217
Del Zanna, G., Dere, K. P., Young, P. R., Landi, E., & Mason, H. E. 2015, A&A, 582, A56
Dey, S., Chatterjee, P., Murthy, O. V. S. N., et al. 2022, NatPh, 18, 595
Erdélyi, R., & Fedun, V. 2007, Sci, 318, 1572
Hansteen, V. H., De Pontieu, B., Rouppe van der Voort, L., van Noort, M., & Carlsson, M. 2006, ApJL, 647, L73
Hassler, D. M., Dammasch, I. E., Lemaire, P., et al. 1999, Sci, 283, 810
Heggland, L., Hansteen, V. H., De Pontieu, B., & Carlsson, M. 2011, ApJ, 743, 142
Iijima, H., & Yokoyama, T. 2017, ApJ, 848, 38
Jiao, F., Xia, L., Li, B., et al. 2015, ApJ, 809, L17
Kanoh, R., Shimizu, T., & Imada, S. 2016, ApJ, 831, 24
Kesri, K., Dey, S., Chatterjee, P., & Erdélyi, R. 2024, ApJ, 973, 49
Kippenhahn, R., & Weigert, A. 1994, Stellar Structure and Evolution (Springer)
Kotani, Y., & Shibata, K. 2020, PASJ, 72, 22
Krieger, A., Timothy, A., & Roelof, E. 1973, SoPh, 29, 505
Lee, J., Wang, H., Wang, J., & Wang, M. 2024, ApJ, 963, 79
Lemen, J. R., Title, A. M., Akin, D. J., et al. 2012, SoPh, 275, 17
Liu, J., Nelson, C. J., Snow, B., Wang, Y., & Erdélyi, R. 2019, NatCo, 10, 3504
Lowder, C., Qiu, J., & Leamon, R. 2017, SoPh, 292, 18
Martinez-Sykora, J., De Pontieu, B., De Moortel, I., Hansteen, V. H., & Carlsson, M. 2018, ApJ, 860, 116
Martinez-Sykora, J., De Pontieu, B., Hansteen, V. H., et al. 2017, Sci, 356, 1269
Martinez-Sykora, J., Hansteen, V., & Moreno-Insertis, F. 2011, ApJ, 736, 9
Mclntosh, S. W., de Pontieu, B., Carlsson, M., et al. 2011, Natur, 475, 477
Morton, R. J., Verth, G., Jess, D. B., et al. 2012, NatCo, 3, 1315
Mumford, S. J., Fedun, V., & Erdélyi, R. 2015, ApJ, 799, 6
Narain, U., & Ulmschneider, P. 1996, SSRv, 75, 453
Pereira, T. M., Carlsson, M., Hansteen, V. H., De Pontieu, B., & Title, A. M. 2014, ApJL, 792, L15
Pereira, T. M. D., Pontieu, B. D., & Carlsson, M. 2012, ApJ, 759, 18
Pesnell, W. D., Thompson, B. J., & Chamberlin, P. C. 2012, SoPh, 275, 3
Priest, E. 2014, Magnetohydrodynamics of the Sun (Cambridge Univ. Press)
Rast, M. P., Bello Gonzalez, N., Bellot Rubio, L., et al. 2021, SoPh, 296, 70
Richardson, I. G. 2018, LRSP, 15, 1
Rosenthal, C. S., Bogdan, T. J., Carlsson, M., et al. 2002, ApJ, 564, 508
Samanta, T., Pant, V., & Banerjee, D. 2015, ApJ, 815, L16
Samanta, T., Tian, H., Yurchyshyn, V., et al. 2019, Sci, 366, 890
Secchi, A. 1877, L'astronomia in Roma nel Pontificato di Pio IX (Tipografia della Pace)
Shen, Y. 2021, RSPSA, 477, 20200217
Shibata, K., & Suematsu, Y. 1982, SoPh, 78, 333
Spruit, H. C. 1974, SoPh, 34, 277S
Srivastava, S., Chatterjee, P., Dey, S., & Erdélyi, R. 2025, ApJ, 989, 39
Sterling, A. C. 2000, SoPh, 196, 79
Sterling, A. C., Shibata, K., & Mariska, J. T. 1993, ApJ, 407, 778
Tian, H., Harra, L., Baker, D., Books, D. H., & Xia, L. 2021, SoPh, 296, 47
Tian, H., Mclntosh, S. W., Wang, T., et al. 2012, ApJ, 759, 144
Tian, H., DeLuca, E., Cranmer, S., et al. 2014, Sci, 346, 1255711
Tsiropoula, G., Tziotziou, K., Kontogiannis, I., et al. 2012, SSRv, 169, 181
Tu, C.-Y., Zhou, C., Marsch, E., et al. 2005, Sci, 308, 519
Wang, Y., Ni, L., Cheng, G., et al. 2025, ApJ, 987, 148
Withbroe, G. L., & Noyes, R. 1977, ARA&A, 15, 363
Yokoyama, T., & Shibata, K. 1995, Natur, 375, 42
Yuan, D., Fu, L., Cao, W., et al. 2023, NatAs, 7, 856
Zaqarashvili, T. V., & Erdélyi, R. 2009, SSRv, 149, 355
Ziegler, U. 2008, CoPhC, 179, 227